Validation of a two-phase multidimensional polymer electrolyte membrane fuel cell computational model using current distribution measurements

Brian Carnes [a],[*], Dusan Spernjak [b], Gang Luo [c], Liang Hao [c], Ken S. Chen [a], Chao-Yang Wang [c], Rangachary Mukundan [b], Rodney L. Borup [b]

[a] Sandia National Laboratories, PO Box 5800, Albuquerque, NM 87185-0382, USA
[b] Los Alamos National Laboratory, MPA-11, PO Box 1663, Los Alamos, NM 87545, USA
[c] ECEC, The Pennsylvania State University, University Park, PA 16802, USA

HIGHLIGHTS

► Model validation using current distribution data is demonstrated using a 3D, multiphase computational fuel cell model.
► Uncertainty in the experimental data is included in the validation in order to improve the model credibility.
► Cell voltage agreement (model and experiment) is within 15 mV.
► Current distribution error is less than 30% at 80 C operation, with errors up to 60% at low temperature (60 C).

ARTICLE INFO

ABSTRACT

Validation of computational models for polymer electrolyte membrane fuel cell (PEMFC) performance is crucial for understanding the limits of the model predictions. We compare predictions from a multiphase PEMFC computational model with experimental data collected under various current density, temperature and humidification conditions from a single 50 cm^2 PEMFC with a 10 × 10 segmented current collector. Both cell voltage and current distribution measurements are used to quantify the predictive capability of the computational model. Several quantitative measures are used to quantify the error in the model predictions for current distribution, including root mean square error, maximum/minimum local error, and local error averaged from inlet to outlet. The cell voltage predictions were within 15 mV of the experimental data in the current range from 0.1 to 1.2 A cm^{-2}, and the current distributions were acceptable (less than 30% local error) except for the low temperature case, where the model over-predicted the current distribution. Particular attention was paid to incorporating experimental variability into the model validation process.

© 2013 Elsevier B.V. All rights reserved.

1. Introduction

In the past two decades a large number of computational models have been presented for modeling polymer electrolyte membrane fuel cells (PEMFC). For reviews of the main models and modeling approaches, see Refs. [1–4] and the references within. While computational models enable unprecedented ability to look into the *in situ* operation of PEMFCs, the limitations of these modeling tools must be understood in order to have confidence in the credibility of the model predictions.

The process of quantifying the degree of credibility of a computational model is known as model validation [5]. Generally validation consists of comparing the output of the model to data from experiments. Here the model has been specifically set up to reproduce the conditions of the experiments; in the case of PEMFCs, this means that the operating conditions, material properties, dimensions, and experimental outputs must be carefully specified in order to provide the best possible inputs to the model. This includes uncertainties, either from random sources (inherent variability) or from lack of knowledge. Comparison of model and experiment with properly quantified uncertainty provides a solid basis to make quantitative determinations.

A wide variety of local (distributed) experimental data has been obtained, which could potentially be used in model validation, including current density [6–11], species (reactants and products)

* Corresponding author. Tel.: +1 505 284 1332; fax: +1 505 284 2418.
E-mail address: bcarnes@sandia.gov (B. Carnes).

[9,10], high frequency resistance (HFR) [7–9], and water balance [10]. Min et al. [12,2] proposed using local current, oxygen concentrations and anode/cathode overpotentials for optimal model validation.

A number of metrics have been used to validate fuel cell models. Probably the most widely used comparison is plotting experimental and simulation data together (either in side-by-side plots or in a single plot). The metric in this case is often qualitative; a more quantitative metric is to plot the differences between simulation and experimental values (the errors) so that their sign and magnitude can be more readily assessed. Finally, inclusion of uncertainties in both experimental data and simulation results should provide the most quantitative assessment of the predictive capability of fuel cell models.

A number of authors have presented model validation results for PEMFCs, including numerous comparisons with cell polarization data. Some authors have even compared their simulation results to the results of other models [10,13]. In this work we are interested in validation using experimental data for both cell polarization and local current density across the active area. Ju and Wang [6] were one of the first groups to perform validation on a cell with a segmented current collector using a 3D computational fluid dynamics (CFD) based model that accounted for single phase gas transport along with electrochemistry and species transport. Hakenjos et al. [7,8] used a 3×15 segmented collector and 14 parallel straight channels to validate a FLUENT®-based fuel cell model using local current and HFR. Lum and McGuirk [13] validated a single-phase, isothermal 3D CFD model of a 14 cm^2 cell that was segmented down the channel. They considered variable relative humidity (RH), flow direction, and stoichiometry, and their validation results required fitting of the model porosity. Recently Fink and Fouquet [14] performed validation using a two-phase model with 3D channels and GDL, and a 1D membrane/catalyst layer model. Their validation data came from a single cell in a 6-cell stack, with area of about 230 cm^2. The validation of local current was done by side-by-side comparison at a base condition, as well as for changing stoichiometry and RH.

The remainder of this paper is organized as follows. First we review the experimental setup and format of the experimental results, including a discussion of data uncertainty. Then we briefly describe the computational model and model parameters, followed by definitions of various validation metrics that we use. We conclude with model validation results for cell polarization and local current density, including the effects of experimental uncertainty.

2. Experimental data

2.1. Hardware and materials

The membrane-electrode-assembly (MEA) used was a GORE® PRIMEA® A510.2/M710.18/C510.4 catalyst-coated membrane [15]. Here the membrane type is GORE® 710 with nominal thickness of 18 μm. The catalyst type was GORE® 510 with Pt loadings of 0.2 mg Pt cm^{-2} on the anode and 0.4 mg Pt cm^{-2} on the cathode. The Pt loadings were modeled by varying the catalyst layer (CL) thickness and reference exchange current density (see Table 4).

Table 1
Control parameters for experiments.

T [°C]	RH [%]			
80	100	75	50	25
60	100	–	50	–

Table 2
Uncertainty quantification for cell voltage at 80 °C/50 RH and 1.2 A cm^{-2}. Note that the overall uncertainty in cell voltage is 16 mV.

Test case	$\overline{V}_j$	$z_{\alpha/2}\sigma_j$	$V_{\min}$	$V_{\max}$
Cell 13	0.609	0.003	0.606	0.612
Cell 14	0.619	0.003	0.616	0.622
Combined	0.614	–	0.606	0.622

The gas diffusion layer (GDL) is SGL®24BC by SGL Technologies GmbH (both cathode and anode side), which includes a microporous layer (MPL) [16]. The compressive force exerted onto the GDL is 120 psi. The GDL was compressed to about 80% of its original (uncompressed) thickness. The MPL was about 20% of the total GDL thickness on average (although the MPL thickness was very nonuniform).

The MEA size is 71 by 71 mm (50 cm^2 cell active area). The flow field and segmented current collector plate are illustrated in Fig. 1. The flow field consists of five-way parallel channels with shared manifolds to enable 180° turns.

2.2. Operating conditions

The main control parameters in the experiments were cell temperature, relative humidity (same value for both anode and cathode) and average current density, which we will abbreviate in what follows as T, RH, and CD, respectively, with units °C, %, and A cm^{-2}. In each experiment, the CD was varied as 0.1, 0.4, 0.8, 1.0, and 1.2 A cm^{-2}. The values of T and RH for all six cases are summarized in Table 1. All other operating conditions were fixed for all experiments. The flow rates were controlled to produce fixed stoichiometries of 1.2 (anode) and 2 (cathode). The back pressure on both anode and cathode was 40 psia.

2.3. Experimental outputs

The experiments were conducted at Los Alamos National Laboratories (LANL) under constant current, with all output quantities recorded over a twenty minute time interval. The output quantities included average cell voltage and current density, local current density distribution, pressure drop and HFR. The last five minutes of each twenty minute time interval included about 80 data points in time and were used for computing time-averaged quantities (cell voltage, local current density, etc.).

At the end of each fixed current interval, the cell was operated at open circuit and the local current measurements were replaced by local temperature measurements, since both current and temperature cannot be measured simultaneously with the present cell hardware. Temperature data was measured for one minute and was averaged over this entire time interval. Here we assume that the measured local temperature is essentially the same as that under the given current load condition. The local temperature data was not used in this study but will be presented in a separate paper.

Table 3
Average cell voltage (V) for all operating conditions.

I [A cm^{-2}]	80 °C				60 °C	
	100 RH	75 RH	50 RH	25 RH	100 RH	50 RH
0.1	0.861	0.862	0.861	0.859	0.861	0.858
0.4	0.788	0.784	0.781	0.777	0.778	0.777
0.8	0.707	0.706	0.697	0.689	0.695	0.688
1.0	0.661	0.660	0.653	0.632	0.650	0.644
1.2	0.617	0.614	0.614	0.576	0.597	0.600

Table 4
Physical dimensions of the computational model.

Dimension	Value	Unit
Membrane thickness	18	μm
CL thickness (anode/cathode)	7/12	μm
MPL thickness	50	μm
GDL thickness	200	μm
Channel height	1	mm
Channel width	1	mm
Land width	1.03	mm
Manifold width	3	mm
Total bipolar plate thickness	3	mm

2.4. Uncertainty quantification

The experimental outputs contain two main sources of uncertainty: (i) transient fluctuations from the time-averaged values and (ii) variability between repeated tests. For a given output f, we computed a best estimate $\bar{f}$ and uncertainty bounds $[f_{min}, f_{max}]$ such that $f_{min} \leq \bar{f} \leq f_{max}$.

Time-averaged quantities were modeled with a Gaussian distribution, with the mean and standard deviation measured by the observed time series values. For a given experiment, uncertainty bounds on the mean value $\bar{f}$ were obtained using a 99% confidence interval (using $\alpha = 0.01$ and $z_{\alpha/2} = 2.576$) around the mean value.

$$[f_{min}, f_{max}] \equiv \left[\bar{f} - z_{\alpha/2}\sigma, \bar{f} + z_{\alpha/2}\sigma \right]. \quad (1)$$

For multiple repeated experiments, we took the best estimate to be the average of the different mean values. The uncertainty was taken to be the extreme values of the uncertainty bounds for each experiment, defined by

$$[f_{min}, f_{max}] \equiv \left[\min_j f_{j,min}, \max_j f_{j,max} \right], \quad (2)$$

where j is the index over the set of experiments. This uncertainty (i.e. repeatability of the experiments), takes into account variations in cell materials (MEA, GDLs) and assembling the cell.

An illustration of the uncertainty quantification of cell voltage at 1.2 A cm^{-2} is shown in Table 2 for two experiments at 80 °C/50 RH. The numerical values used to compute the overall average cell voltage (about 0.6 V) and uncertainty bounds are reported, from which we see that uncertainty from temporal fluctuations is about 3 mV, while variability between tests is about 10 mV. In this case, the variability between experiments is larger than the transient fluctuations.

2.5. Polarization curves

We present in Table 3 the average cell voltage (in Volts) for each of the six operating conditions and five current densities. Uncertainty between time averages of two cells was small, usually less than 5–15 mV. We see that for lower current densities (less than 0.8 A cm^{-2}), the operating conditions have a negligible effect on cell voltage. However, reducing the temperature and RH from the 80 °C/50 RH operating point can reduce the cell voltage 15–40 mV (80 °C/25 RH) or 15–20 mV (60 °C/50 RH) at higher current densities. Also, because the effect of RH is only significant for 50 RH or less, we limit our validation to this low humidity case. In a forthcoming study we validate our model under fully humidified conditions using liquid water data from neutron imaging. Based on the above comments, we therefore focus on the following operating conditions for cell voltage validation: 80 °C/50 RH, 80 °C/25 RH, and 60 °C/50 RH. Furthermore, since the uncertainty in cell voltage was less than 15 mV, we will use this value also as a benchmark to assess validation of cell voltage.

2.6. Current density distribution

In this section we discuss the uncertainty in the experimental current distribution data. In colorized distribution plots of current density and uncertainty hereafter, matrix elements correspond to the segments in the current collector, as shown in Fig. 1.

One issue with local current distribution data is that the measurements are susceptible to variable contact resistances, which can pollute the results. In addition, at the inlet/outlet locations, no measurements are available because the channels penetrate these segments. To overcome these issues, we implemented a simple Laplace smoothing that we applied to the time-averaged 10×10 current density arrays. If $I_{i,j}$ is the current at a point (i, j) in an array, the smoothed value $I^s_{i,j}$ for a single iteration is determined by

$$I^s_{i,j} = (1-\omega)I_{i,j} + \omega\frac{1}{4}\{I_{i-1\,j} + I_{i+1\,j} + I_{i,j-1} + I_{i,j+1}\}, \quad 1 \leq i,j \leq 10$$

where ω is a relaxation parameter.

For locations at the boundaries ($i, j = 1$ or 10), we choose the values outside the array by reflection. For example, to compute the smoothed value in the upper left corner $I^s_{1,1}$ at location (1,1) in the array, we define the values to the left and top as

$$I_{0,1} = I_{2,1}, \quad I_{1,0} = I_{1,2},$$
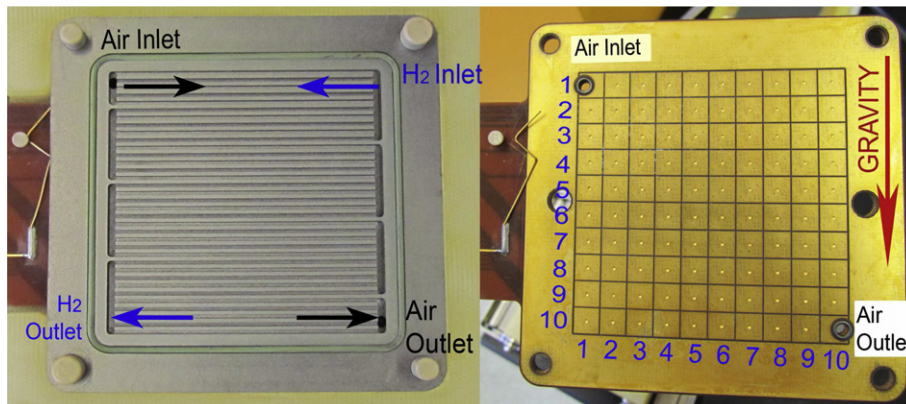
Fig. 1. Bipolar plate with flow field (left) and 10×10 segmented current collector plate (right).

respectively. This insures that the smoothing of boundary values only uses the adjacent values within the array.

In Fig. 2 we illustrate the procedure applied to a matrix at 80 °C/50 RH/1.0 CD using three smoothing iterations and $\omega = 0.9$.

We see that the smoothing has removed oscillations present in the raw experimental data arrays from segments with high contact resistance or inlet/outlets (where no current density is measured) and that the characteristics (minimum, maximum, etc.) are much easier to discern using the smoothed array. The same smoothing parameters were used in all subsequent plots of measured current distribution.

In Fig. 3, we present the distribution of relative uncertainty in local current density for the 80 °C/50 RH case at 0.1 and 1.0 A cm^{-2}. The local uncertainty is calculated exactly as we calculated the uncertainty in cell voltage for each point in the 10×10 array. In contrast to the cell voltage data, the variability between experiments can be as large as 15% at some locations, while less than 5–10% at most locations. Because of this, we have included metrics that exclude outliers in order to compute bounds on the current distribution predictions of the model. It is interesting to note that in both cases, the highest uncertainty occurs in the lower right corner near the outlets.

3. Computational model

3.1. Model details

The computational model used in this study was developed by the group of C.-Y. Wang and collaborators at The Pennsylvania State University (PSU) and has been presented in a number of references [17–19]. The current implementation uses ANSYS/FLUENT® with most of the model implemented in a library of user defined functions (UDFs). The primary equations solved are conservation of mass, momentum, energy, species and electrical/ionic charge.

Two-phase flow in the porous zones is modeled using the multiphase mixture model of Wang and Cheng [20] using primary variables of mixture pressure, velocity, and species concentration, as well as temperature and electrical/ionic potentials. A key variable calculated from the solution process is the liquid water saturation in porous zones (catalyst layers and diffusion layers), which is the average volume fraction of pores occupied by liquid water. While the model includes liquid transport in the channels [21], in this paper we restrict ourselves to mist transport in the channels, since we are only validating against the low humidity data (RH = 50

or 25). This is because the experimental data exhibits low sensitivity to T or CD for RH greater than 50.

3.2. Model input parameters

In this section we briefly describe the model input geometric dimensions and parameters, which are summarized in Tables 4 and 5, respectively. The geometric dimensions not discussed are taken from drawings from the manufacturer of the bipolar plates (balticFuelCells GmbH). Thicknesses of the membrane and catalyst layers were measured from SEM cross-sections as reported in a related work [22].

The membrane model used for conductivity, water diffusion coefficient, electro-osmotic drag, sorption isotherms and saturation pressure is the model of Springer et al. [23], with the membrane water diffusivity scaled by a factor of 0.7. The variable membrane density model is given by Eq. 17 in West and Fuller [24] with a fixed membrane thickness of 18 μm. The thermal conductivity of the membrane was based on PSU data and was taken to be 0.95 W m^{-1} K for this study.

In the catalyst layers, the main parameters (Table 5) used in the Butler–Volmer kinetics are the reference reactant concentrations $c_{H2}^{ref}, c_{O2}^{ref}$, reference exchange current densities (volumetric) j_a^{ref}, j_c^{ref}, and transfer coefficients α_a, α_c. The cathode reaction rate j_c^{ref} was estimated from several experimentally obtained parameters using the equation

$$j_c^{ref} = j_{c,surf}^{ref}\left(\frac{m_{Pt}}{t_c}\right)\text{ECSA}, \qquad (3)$$

where $j_{c,surf}^{ref}$ is the surface reaction rate for oxygen reduction on platinum, m_{Pt} is the platinum loading, t_c is the thickness, and ECSA is the electrochemical surface area [22].

The reaction rate j_c^{ref} uses a parameter E_c based on PSU data to represent the temperature dependence of the cathode reaction

$$j_c^{ref} = j_c^{ref,353.15}\exp[-E_c(1/T - 1/353.15)].$$

The thicknesses of the catalyst layers were determined from SEM images obtained at LANL [22].

The GDL (SGL24BC) contains an MPL layer, which is modeled as a separate layer in the model. We determined the thicknesses of each layer using a total substrate thickness of 250 μm with a 50 μm thick MPL.
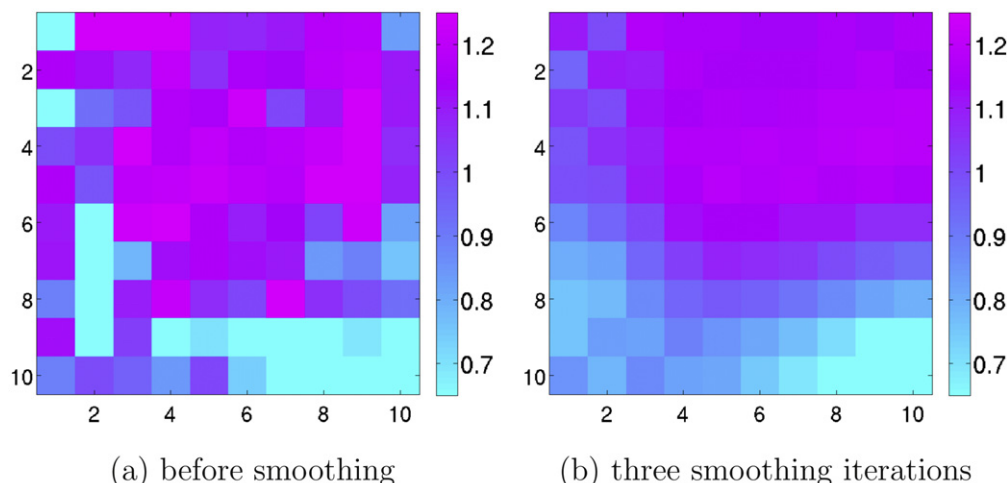

(a) before smoothing   (b) three smoothing iterations

Fig. 2. Example of smoothing current distribution data (A cm^{-2}) at 80 °C/50 RH/1.0 CD.
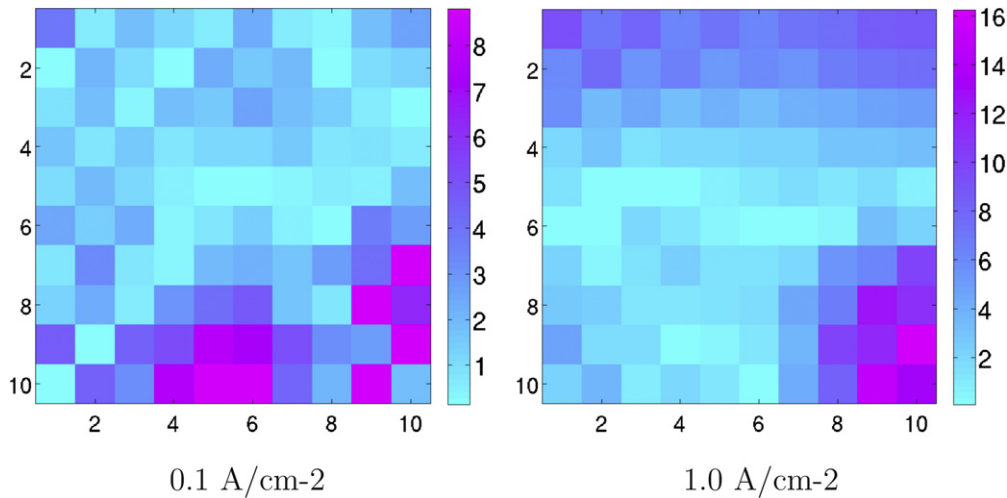
0.1 A/cm-2   1.0 A/cm-2

Fig. 3. Local percent relative uncertainty for current distribution for 80 °C/50 RH, at two different values of CD.

3.3. Computation of current density distribution

The spatial resolution of the experimental data is about 0.5 cm², at which average values of local current and temperature can be obtained (although not simultaneously). In contrast, the computational model can have resolutions (using computational grids) that are much smaller, ranging from 0.01 to 0.25 mm². In order to compare the model predictions with the data, we must average the model prediction of current over a number of grid cells to match the resolution of the experimental data. A postprocessing script was written to average the computed current density along a 10 × 10 grid corresponding to the collector plate shown in Fig. 1.

3.4. Numerical uncertainty from mesh convergence

In order to estimate the uncertainty in the model arising from numerical error (lack of mesh convergence), we produced solutions on several different grids. For example, we compared the solution outputs (cell voltage and local current density) computed using two different grids. The coarse (fine) mesh contained about 1.5 M (2.4 M) cells with 5 × 5 (6 × 6) cells through the channels; the fine mesh contained about 50% more cells through the thickness of each layer.

In Table 6 we report the uncertainty in cell voltage for the case of 80 °C, 50 RH at two different current densities. We see that the change in cell voltage is always less than 5 mV; we thus conclude that numerical error in cell voltage is sufficiently small for validation (since our experimental uncertainty was less than 15 mV).

We also calculated the numerical uncertainty (percent relative change between two grids) in local current density at the same operating conditions (80 °C/50 RH) and at two different current densities of 0.8 and 1.2 A cm⁻². The uncertainty in local CD is estimated to be no more than 4% at 0.8 A cm⁻² and no more than 10% at 1.2 A cm⁻². The regions with the largest numerical error appear to be the near the inlet and along the edges of the active area. Compared to cell voltage, the numerical error can thus be much larger; this situation parallels the increased variability in the experimental current data distribution over the fairly consistent cell voltage data (see Fig. 3).

Because the uncertainty in the experimental current distribution data is about 8–15%, we conclude that the 4–10% uncertainty from numerical error is acceptable for the grids used in this study.

4. Validation metrics

4.1. Cell voltage

For any operating condition (T, RH and CD) we have a cell voltage from the experiment, denoted V^{exp}, and from the simulation, denoted V. In the absence of any uncertainty we can define the validation metric for the error in voltage (EV) between simulation and experiment using the difference

$$EV \equiv V - V^{exp}. \tag{4}$$

Table 5
Material parameters.

Parameter	Value	[Units]
ε	0.6	[−]
K	1e-12	[m²]
θ	92.0	[°]
k_{MEM}	0.95	[W m⁻¹ K]
k_{CL}	1.0	[W m⁻¹ K]
k_{MPL}	1.0	[W m⁻¹ K]
k_{GDL}	1.0	[W m⁻¹ K]
k_{BP}	20	[W m⁻¹ K]
σ_{CL}	3e3	[S m⁻¹]
σ_{MPL}	3e3	[S m⁻¹]
σ_{GDL}	3e3	[S m⁻¹]
σ_{BP}	2e6	[S m⁻¹]
c_{H2}^{ref}	40	[mol m⁻³]
c_{O2}^{ref}	40	[mol m⁻³]
j_a^{ref}	1.2e10	[A m⁻³]
$j_c^{ref,353.15}$	4.8e3	[A m⁻³]
$j_{c,surf}^{ref,353.15}$	3.85e-4	[A m⁻²]
ECSA	60	[m² g⁻¹ Pt]
E_c	8.0e3	[J mol⁻¹]
α_a, α_c	2,1	[−]
n (Bruggman)	2.8	[−]
$R_{GDL/BP}$	0.1e-6	[Ω m²]
$R_{CL/MPL}$	0.25e-6	[Ω m²]

Table 6
Numerical error in cell voltage. Operating conditions are 80 °C and 50 RH.

Current [A cm⁻²]	5 × 5 mesh [V]	6 × 6 mesh [V]	Error [mV]
0.1	0.85235	0.85264	0.3
0.4	0.77891	0.78101	2.1
0.8	0.72608	0.72688	0.8
1.0	0.70176	0.70453	2.8
1.2	0.67807	0.68248	4.4

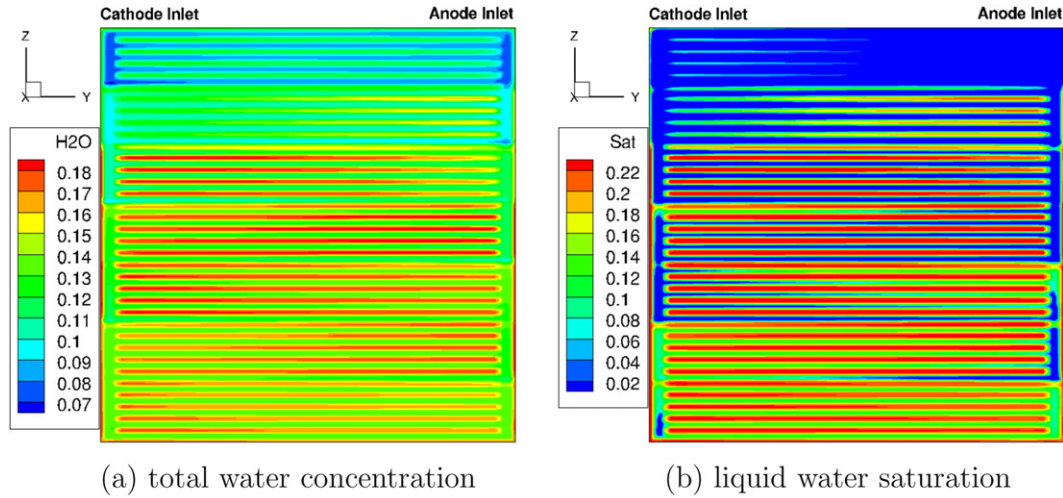(a) total water concentration

(b) liquid water saturation

Fig. 4. Mid-plane of the cathode GDL at 80 °C, 50% RH and 1.0 A cm^{-2}: water concentration (mol m^{-3}) and liquid saturation (−).

However, as discussed in Section 2.4, variability in the experimental data can be modeled using an interval $[V_{\min}^{\exp}, V_{\max}^{\exp}]$. In this case we can define the validation metric UEV as the signed distance between V and this interval

$$
\text{UEV} \equiv \begin{cases} V - V_{\max}^{\exp} & V > V_{\max}^{\exp}, \\ V - V_{\min}^{\exp} & V < V_{\min}^{\exp}, \\ 0 & \text{else}. \end{cases} \tag{5}
$$

Thus if $V_{\min}^{\exp} \leq V \leq V_{\max}^{\exp}$, then the metric returns zero, since the simulation value lies within the uncertainty. Positive/negative metrics imply overshoot/undershoot of the interval of uncertainty around the experimental data.

4.2. Current density distribution

The validation metrics for current density distribution are based on the local errors in the current density defined by

$$
E_i \equiv I_i - I_i^{\exp}, \quad i = 1, \ldots, N \tag{6}
$$

where $N = 100$ is the total number of segments. The metrics are the root mean square relative error,

$$
\text{RMS} \equiv \frac{100}{I_{\text{avg}}} \left(\sum_i \frac{|E_i|^2}{N} \right)^{1/2}, \tag{7}
$$

and minimum/maximum of the relative error,

$$
\text{MIN} \equiv P_5(\{100E_i/I_i\}_i), \tag{8}
$$

$$
\text{MAX} \equiv P_{95}(\{100E_i/I_i\}_i), \tag{9}
$$

where P_r denotes the r-th percentile of a set of data ($0 \leq r \leq 100$). We have excluded the bottom/top 5% of the errors, in order to exclude extreme values which may be associated with noise in either the experiment or simulation.

We also define metrics based on averaging the local segmented current along each horizontal row of segments (as shown in Fig. 1) in order to consider the average current along the overall flow direction from inlet to outlet (top to bottom). These are defined
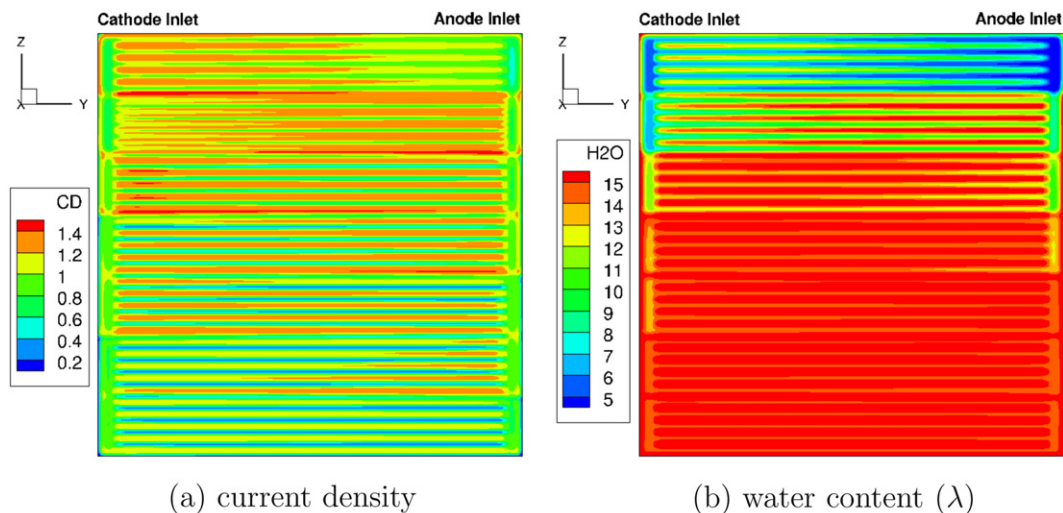

(a) current density

(b) water content (λ)

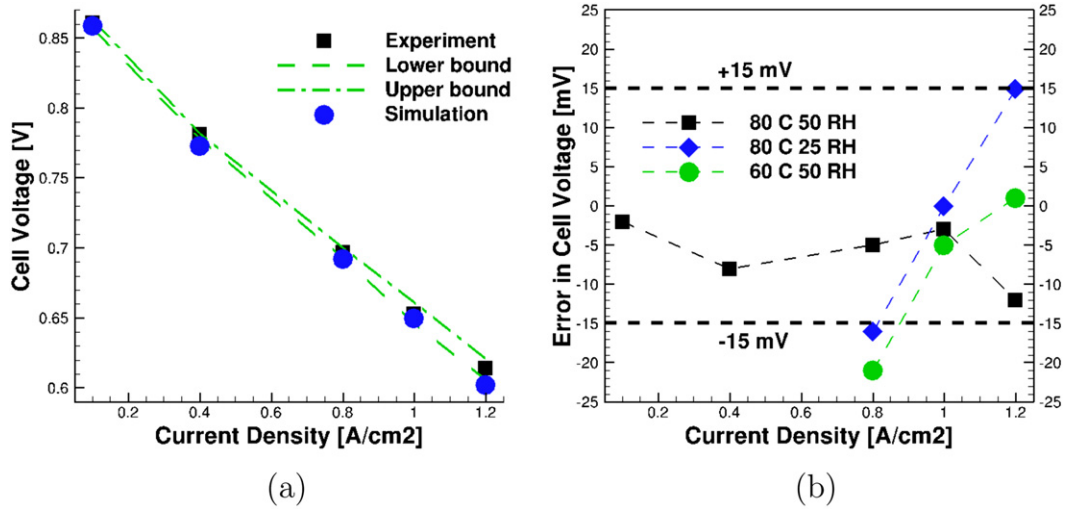**Fig. 5.** Mid-plane of the membrane: CD and water content (λ).

Fig. 6. Validation of cell polarization curves under experimental uncertainty. (a) Comparison of experimental and simulation curves for 80 °C/50 RH. (b) Errors between simulation and experiments for various operating conditions.
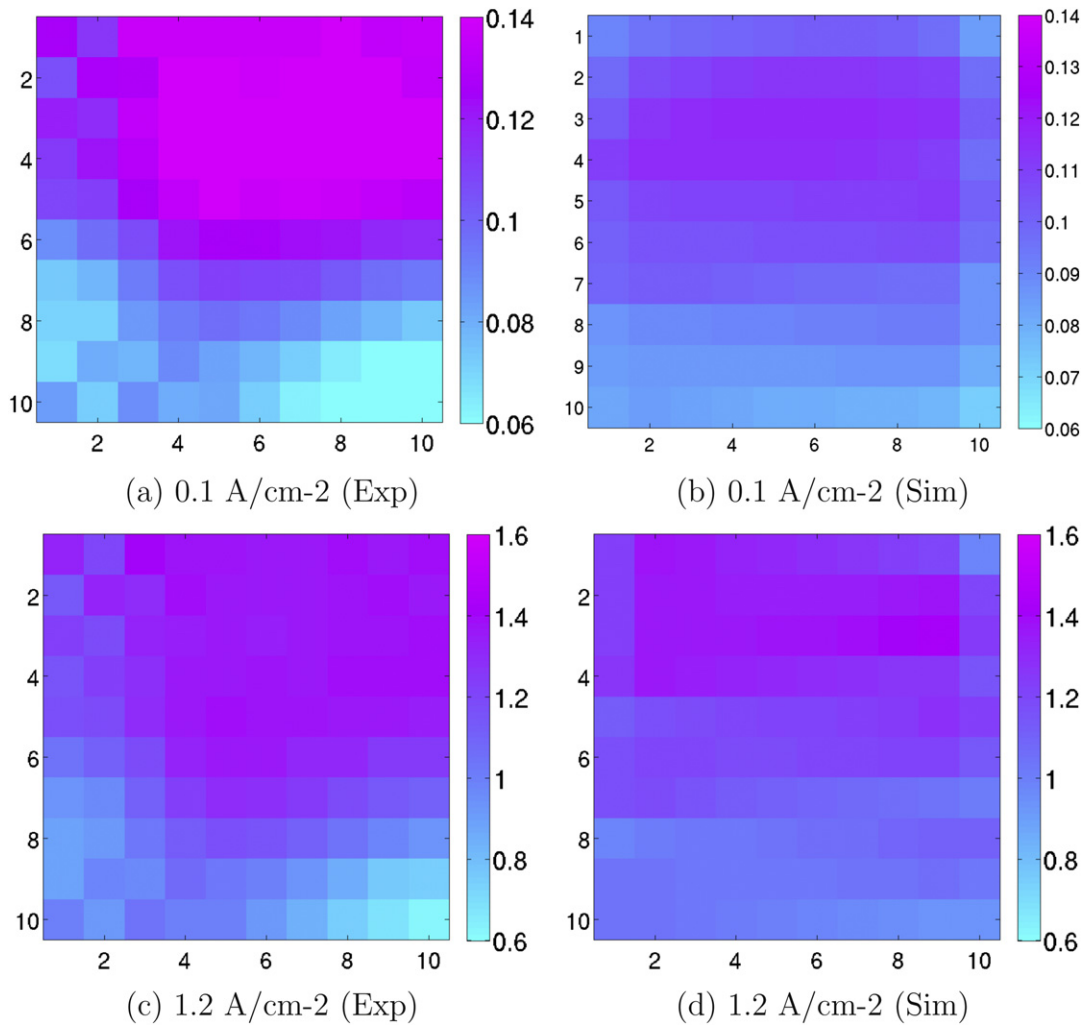

Fig. 7. Validation of average CD effect on local CD distribution (A cm^{-2}) for 80 °C/50 RH. Experimental data is on left with simulation data on right.

exactly as in Eqs. (7)–(9) except that we replace the $N = 100$ data points by the $\sqrt{N} = 10$ row averages of the simulation and experimental data.

Finally we note that inclusion of experimental uncertainty in local current data can easily be done by extending the simple definition of the error using the same formula for cell voltage in (5).

5. Results

5.1. Example simulation output

Before we present the validation results, we begin with some representative results of the simulation output obtained using the computational model. We focus on a specific operating point at 80 °C, 50 RH and 1.0 CD.

In Fig. 4 we plot the concentration of total water and liquid water saturation along the mid-plane of the cathode GDL. The total water concentration increases from inlet to outlet, mainly from the product water. Liquid water accumulates in the lower half of the GDL, predominantly under the land areas and along the edges of the cell.

In Fig. 5 we plot the distribution of CD and water content λ (number of water molecules per sulfonic acid site in the membrane) in the center plane of the membrane. The region of maximum current is in the lower center area, similar to the

experimental data as we will see shortly. We also see an increase in water content in the lower part of the membrane, toward the outlet, as a result of the increased water production. At the top, near the inlet, the membrane is driest, due to the dry (50 RH) inlet conditions and lower CD. Local drying also occurs under the manifolds due to the increased flow rates in these areas.

5.2. Validation using cell voltage

In Fig. 6 we compare the model prediction of cell voltage against the experimental data. Here for the case of 80 °C/50 RH the experimental data have been plotted with the estimated uncertainty bounds in Fig. 6(a) in order to more precisely assess the validation. We also plot the error for all cases in Fig. 6(b). For the case of 80 °C/50 RH the errors is less than 15 mV, and in all cases it is within 20 mV of the experimental voltage. For the error metrics, uncertainty is included, although it was not large for cell voltage.

5.3. Validation using current distribution

We present three kinds of validation results for current distribution: qualitative validation of trends as CD, RH and T are varied; quantitative validation of current distribution (using RMS or min/max error); and quantitative validation of average current distribution from inlet to outlet.
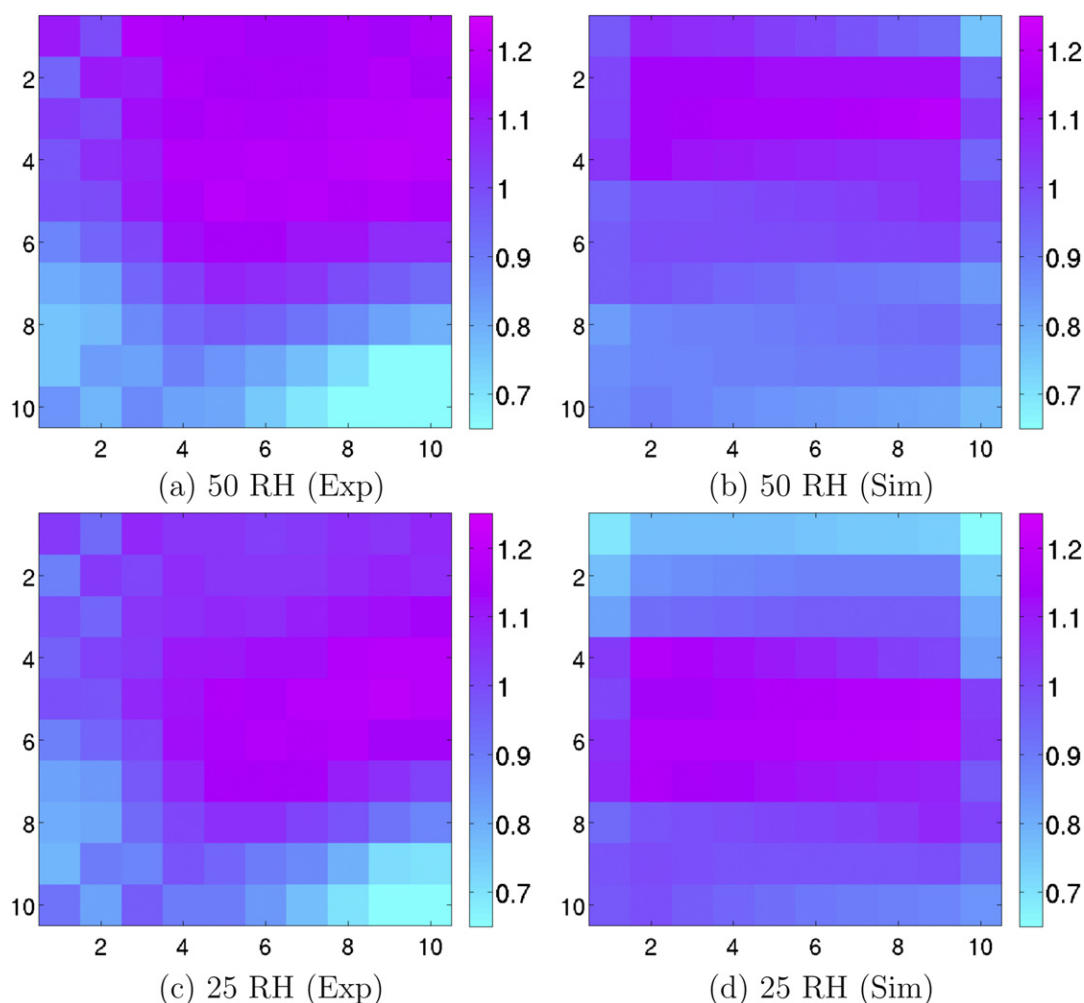

Fig. 8. Validation of RH effect on local CD distribution (A cm^{-2}) for 80 °C and 1.0 cm^{-2}. Experimental data is on left; simulation data is on right.
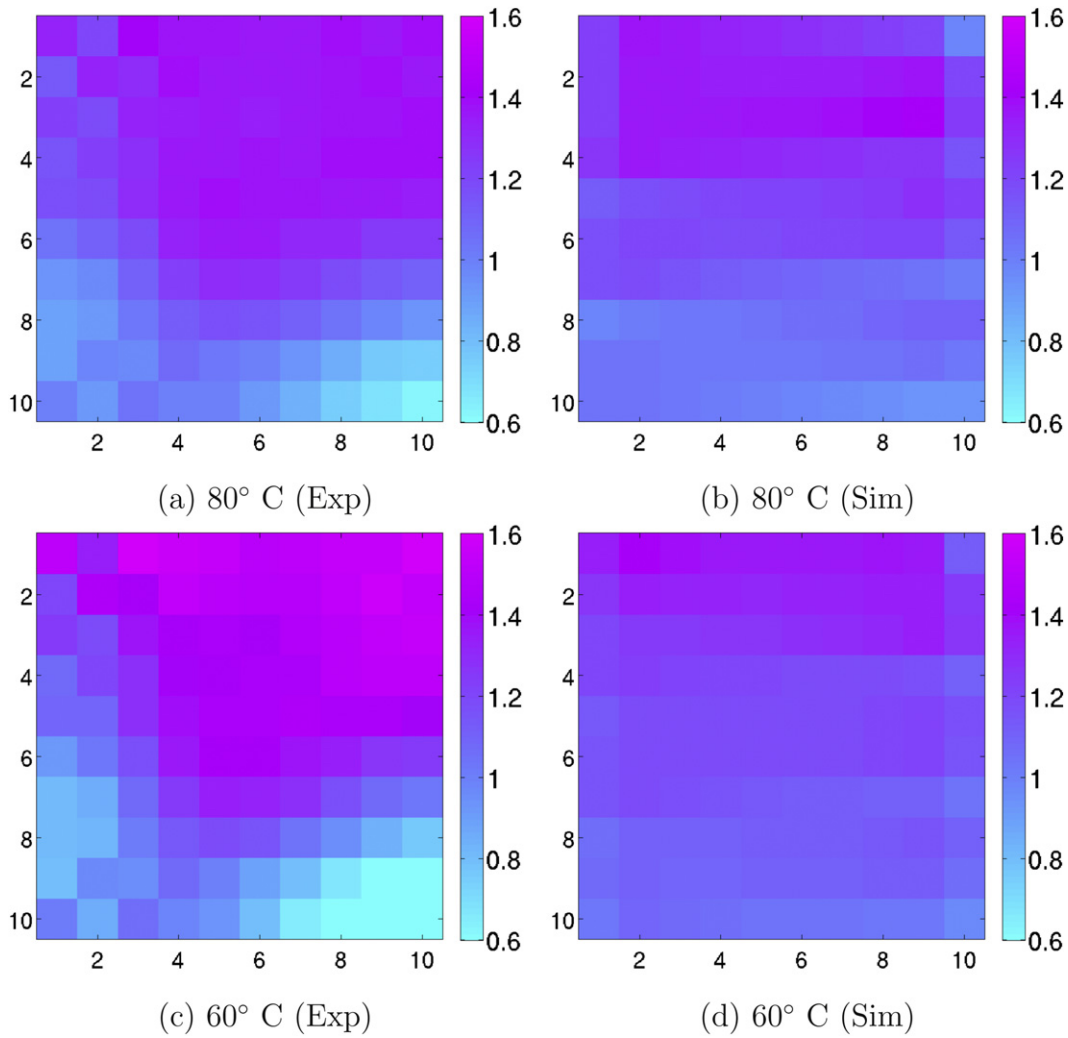
Fig. 9. Validation of *T* effect on local CD distribution (A cm^{-2}) for 50 RH and 1.2 cm^{-2}. Experimental data is on left with simulation data on right.

In Fig. 7(a and c) we see a local maximum current density in the middle- to upper-right part of the cell for the experimental data. The maximum current ranges from about 120 to 150% of the average current density. We observe that at both low and high values of the average CD, the location of the maximum CD is nearly the same for both experiment and simulation, either in the upper-right or middle-right of the cell. In this case (and in others below), we note that the experimental data generally has a local decrease in
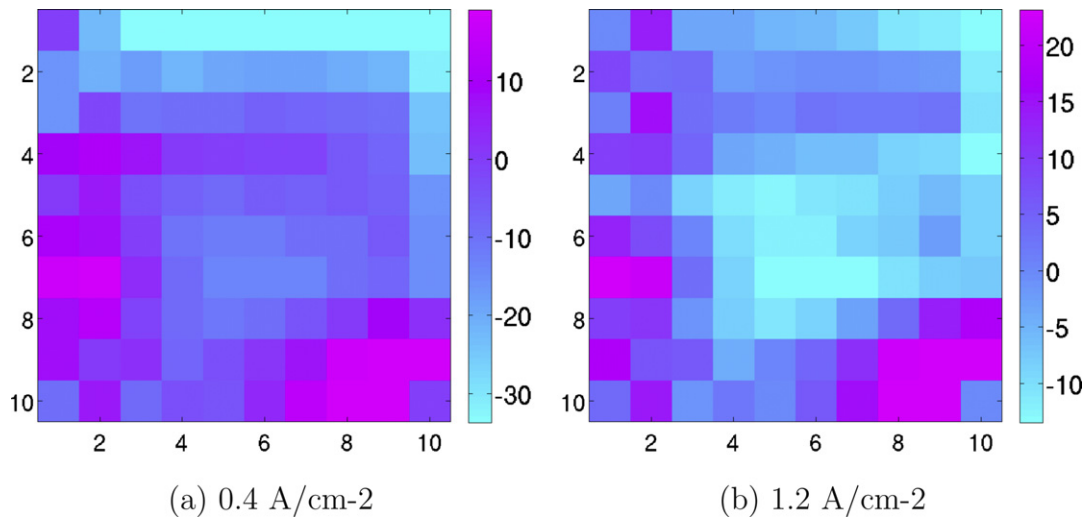

Fig. 10. Relative error (experiment minus simulation) in local CD at 80 °C/50 RH. Percentiles used for cutoffs were 5/95 for lower/upper bounds.
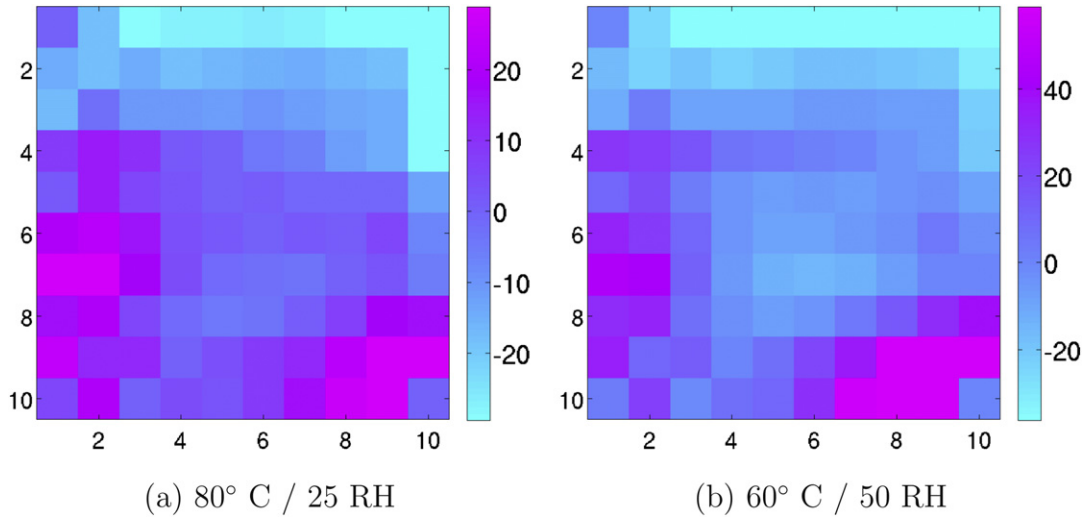
Fig. 11. Relative error (experiment minus simulation) in local CD at 1.0 cm^{-2}. Percentiles used for cutoffs were 5/95 for lower/upper bounds.

current in the bottom-right corner, near the location of the cathode outlet. This feature is not evident in any of the simulation results. One possible explanation for this discrepancy could be channel flooding, which the model used cannot predict, since we are not activating the two-phase channel sub-model.

In Fig. 8(a and c) we plot the effect of decreasing RH at CD = 1.0 A cm^{-2} and 80 °C for the experimental data. Here we see that the local maximum CD shifts downward with decreasing RH from 50 to 25. We observe a similar shift in maximum CD in the simulation data (b, d), along with similar values of the maximum CD. However, the simulation again does not predict the drop in local current near the cathode outlet. The model also underpredicts the current along the top row of segments, near the inlets, at 25 RH. This may be to excessive drying in the model near the inlet.

In Fig. 9(left panels) we plot the effect of temperature at 50 RH and 1.0 CD for the experimental data. We see that as the temperature is decreased from 80 to 60 °C, the maximum CD shifts toward the top (inlets). We observe a similar shift for the simulation data, although the current distribution is much more uniform at 60 °C, failing to reach the same maximum or minimum CD. The difficulty with the predictions at low temperature could be due to the large amount of temperature-dependent properties in the model; some

of these properties may be well calibrated at 80 °C, but less so at other temperatures. Another possibility is the choice of boundary conditions. We assume in this work that a uniform temperature boundary condition is valid; however, the cell surface in fact has some variation in temperature.

In Fig. 10 we plot the distribution of percent relative error in the prediction of segmented (i.e. local) current for the case of 80 °C/50 RH at two different current densities. The errors are generally within 20% of the experimental values, with largest underestimation along the top row of segments (inlet region) and largest overestimation in the lower left area (near the anode outlet). Such plots of actual errors can be useful in pinpointing regions of maximum disagreement between simulations and experiments.

In Fig. 11 we present the distribution in CD error at a fixed average CD of 1.0 A cm^{-2} at two other operating conditions (80 °C/25 RH and 60 °C/50 RH). At 25 RH, the local errors are again generally within 20% of the experimental values. However, at 60 °C, overprediction of local current reaches 60% near the outlet and on the left side of the cell.

In Fig. 12(a) we plot global error metrics for RMS relative error for a number of operating conditions. These are used to integrate the local information in Figs. 10 and 11 into global data that can be more easily summarized. For example, at lower CD, the errors are
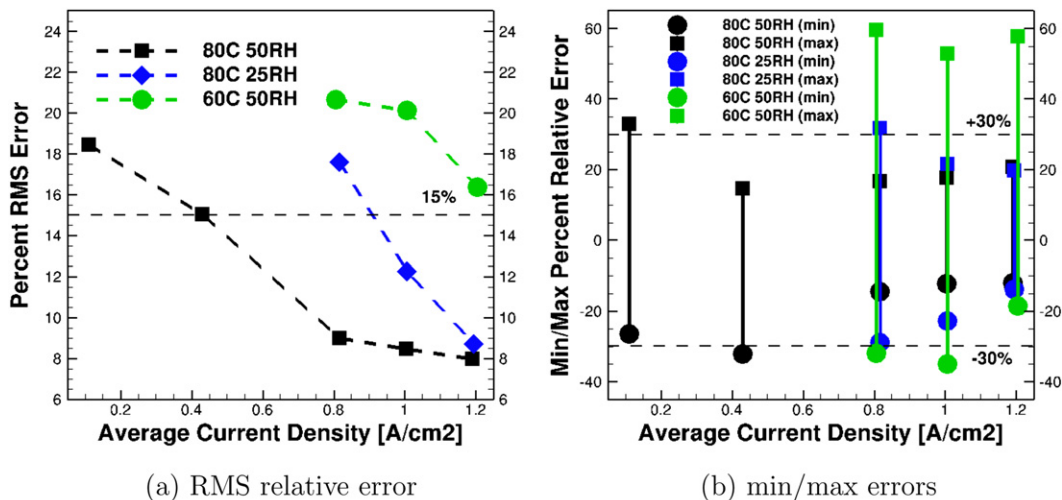

Fig. 12. Error metrics for current distribution at various operating conditions.
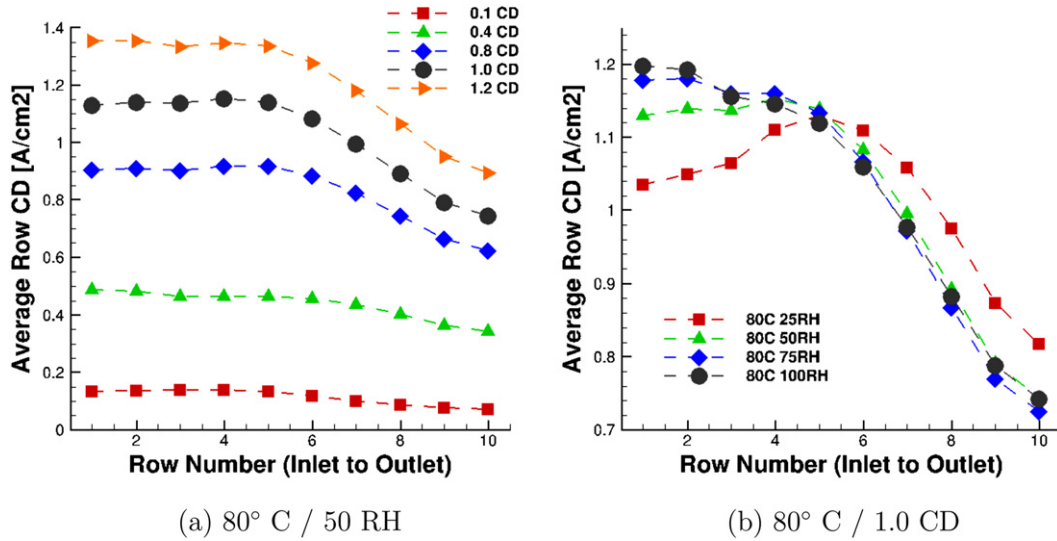
Fig. 13. Averaged current density (experimental data) from top to bottom (inlet to outlet).

highest, which is expected since we are computing relative errors. However, at higher CD, we maintain relative errors generally less than about 15%, with the exception of the 60 °C/50 RH case, where the errors are about twice as large as the other two cases. As stated early, the model appears to suffer from calibration issues associated with temperature-dependent properties, hindering its predictive capability over a wide range of temperatures. We emphasize that rigorous characterization of all material properties and constitutive models should be able to alleviate most of these problems, since the model contains almost all of the fundamental physics.

In Fig. 12(b) we plot error metrics for min/max relative error for a number of operating conditions. For the 80 °C conditions, the upper/lower bounds on the errors are about +/−30%. However, at 60 °C, the upper bound on the error increases to 60% with about the same lower bound, as indicated in error distribution in Fig. 11(b). The min/max error metrics are more stringent (and generally have higher errors in our case), but should be included to show where the model performs worst.

In Fig. 13 we plot the row averages of the local current density (experimental data) from top to bottom, which is aligned with the overall flow direction from inlet to outlet. In Fig. 13(a) we see that for fixed RH = 50, the current density is constant in the top half of the cell (rows 1 through 5), with a value about 15% higher than the cell average. In the bottom (i.e. downstream half of the cell − rows 6 through 10), the current density decreases. In Fig. 13(b) we hold the current density at 1.0 A cm^{-2} and consider the effect of RH. In the upstream (top) half of the cell, we see a clear decrease in current density as RH is decreased. At RH of 50 and especially 25, the inlet region (rows 1 through 4) is under-humidified, resulting in lower local current density due to overly dry conditions. Humidity increases downstream, resulting in similar row-averaged values for the bottom half of the cell for most RH conditions. Such current density distribution correlates well with the humidity distribution plots given in Figs. 4 and 5.

In Fig. 14(a) we plot error metrics for average CD from inlet to outlet (top to bottom) for the base case 80 °C/50 RH. We see that in this metric, we are able to exhibit smaller errors, generally in the range of +/−15% away from the inlet (row 1) and outlet (row 10). These errors are better than those in Fig. 12, which were typically up to 30%. At the inlet/outlets, the errors can be as large as −40% (underestimates of local CD). In Fig. 14(b) we plot the same error metric for three different operating conditions (all at 1.0 CD). Away from the inlet and outlet regions, the errors are similar for the three operating conditions, but with even larger errors at the inlet/outlet
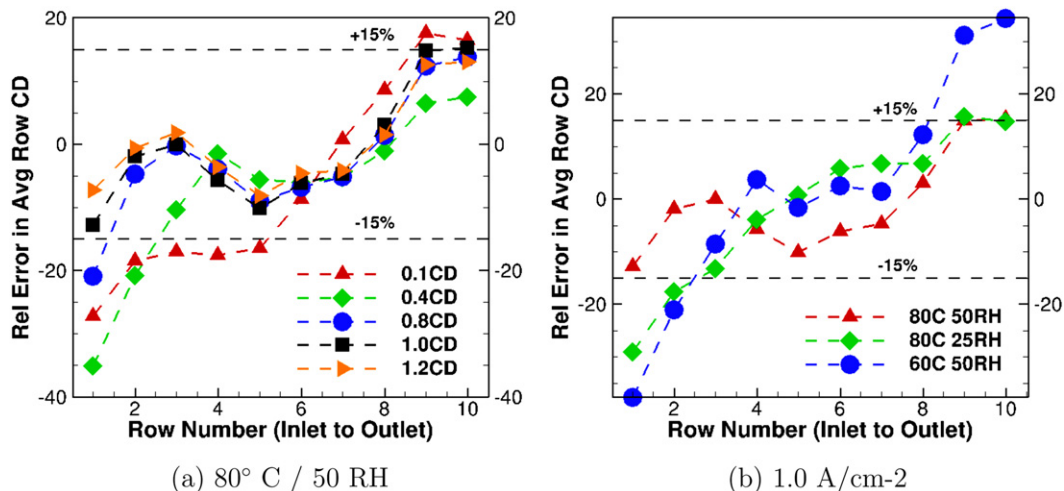

Fig. 14. Relative errors in average CD from inlet to outlet. Averaging is done along rows with inlet at row 1.

regions. We conclude that the increase in the errors for the 60 °C condition shown in Fig. 12(b) is mainly a result of larger errors in the inlet/outlet regions. As mentioned above, these inlet/outlet errors could be from incorrect temperature boundary conditions, temperature-dependent material properties, or possibly liquid water formation in the channels.

6. Conclusions

We have presented model validation results based on current distribution data and a multiphase PEMFC computational model. The cell voltage validation results were acceptable, generally with errors less than 15 mV. For current distribution validation, we presented the results using a number of validation metrics, including RMS error, min/max local error, and averaged errors along the flow direction from inlet to outlet. The best results obtained were at the 80 °C condition (both 25 and 50 RH), where the local error was less than 30% and RMS error was less than 15%. Larger errors at 60 °C/50 RH (up to 60% overestimation of local current) appear to be localized to the inlet/outlet regions. These errors may be the result of incorrect temperature boundary conditions, improperly calibrated temperature-dependent material properties, liquid water in the gas channels, or some other unknown cause.

Inclusion of uncertainty in the validation metrics was possible because of repeated experimental data. The uncertainty allowed us to more precisely quantify the validity of the computational model, through the use of intervals of uncertainty around the experimental data, which represent the range of variability present in the experiments and measurements.

We conclude with several remarks and suggestions for future work. First, model validation requires a careful interaction between modelers and experimentalists; experimental conditions must be faithfully reproduced in simulations, model input characterization requires knowledge of the materials used (especially with temperature-dependent material properties), and uncertainty in experimental measurements must be quantified. The latter was achieved in this work by repeating the characterization tests in several cells re-assembled using new materials (MEAs and GDLs).

Second, while cell voltage data is a good starting point for validation models, other outputs such as current distribution data should be used. The higher the resolution in such local data, the greater the need becomes to account for the inherent uncertainty in the data and in the computational models.

For future work, we intend to further integrate the validation metrics into forms that can be presented succinctly, as well as define additional well-characterized experiments suitable for model validation. Further, some parameters in the present model will be discussed in more detail, taking into account the predicted water distribution and using neutron imaging measurements as an additional validation metric.

Acknowledgments

Nomenclature

c_{H2}^{ref}	reference hydrogen concentration
c_{O2}^{ref}	reference oxygen concentration
ECSA	electro-chemical surface area
E_c	temperature coefficient in j_c^{ref}
j_a^{ref}	reference anode exchange current density
$j_c^{ref,353.15}$	reference cathode exchange current density
$j_{c,surf}^{ref,353.15}$	reference surface Pt exchange current density
K	permeability
k	thermal conductivity
N	number of segments
n	Bruggeman exponent
R	contact resistance
RMS	root mean square error
V	cell voltage

Greek symbols

λ	membrane water content
ε	porosity
θ	contact angle
σ	electrical conductivity
α_a, α_c	transfer coefficients

Subscripts/superscripts

ref	reference value
exp	experimental
sim	simulation

References

[1] S. Mazumder, J. Cole, J. Electrochem. Soc. (2003).
[2] W. Tao, C. Min, X. Liu, Y. He, B. Yin, W. Jiang, J. Power Sources 160 (2006) 359–373.
[3] P. Sui, S. Kumar, N. Djilali, J. Power Sources 180 (2008) 410–422.
[4] T. Berning, M. Odgaard, S. Kaer, J. Electrochem. Soc. 156 (2009) B1301–B1311.
[5] W. Oberkampf, C. Roy, Verification and Validation in Scientific Computing, Cambridge University Press, 2010.
[6] H. Ju, C.-Y. Wang, J. Electrochem. Soc. 151 (2004) A1954–A1960.
[7] A. Hakenjos, K. Tüber, J. Schumacher, C. Hebling, Fuel Cells 3 (2004) 185–189.
[8] A. Hakenjos, C. Hebling, J. Power Sources 145 (2005) 307–311.
[9] Q. Dong, M.M. Mench, S. Cleghorn, U. Beuscher, J. Electrochem. Soc. (2005).
[10] P. Sui, S. Kumar, N. Djilali, J. Power Sources 180 (2008) 423–432.
[11] H. Ly, E. Birgersson, M. Vynnycky, A. Sasmito, J. Electrochem. Soc. (2009).
[12] C. Min, Y. He, X. Liu, B. Yin, W. Jiang, W. Tao, J. Power Sources 160 (2006) 374–385.
[13] K. Lum, J. McGuirk, J. Power Sources 143 (2005) 103–124.
[14] C. Fink, M. Fouquet, Electrochim. Acta 56 (2011).
[15] S. Cleghorn, J. Kolde, W. Liu, Handbook of Fuel Cells: Fundamentals, Technology and Applications, vol. 3, John Wiley & Sons, pp. 566–575.
[16] SIGRACET GDL 24 & 25 Series Gas Diffusion Layer, SGL Technologies GmbH, 2007. Technical Report.
[17] S. Um, C. Wang, J. Power Sources 124 (2004) 40–51.
[18] U. Pasaogullari, C. Wang, K. Chen, J. Electrochem. Soc. 152 (2005) A380–A1582.
[19] S. Basu, C.-Y. Wang, K.S. Chen, J. Electrochem. Soc. 156 (2009) B748–B756.
[20] C.-Y. Wang, P. Cheng, Int. J. Heat Mass. Transf. 39 (1996) 3607–3618.
[21] Y. Wang, S. Basu, C.-Y. Wang, J. Power Sources 179 (2008) 603–617.
[22] D. Spernjak, J. Fairweather, R. Mukundan, T. Rockward, R. Borup, J. Power Sources 214 (2012) 386–398.
[23] T. Springer, T. Zawodzinski, S. Gottesfeld, J. Electrochem. Soc. 138 (1991) 2334–2342.
[24] A. West, T. Fuller, J. Appl. Electrochem. 26 (1996) 557–565.